X-ray polarization: A view deep inside cosmic ray driven turbulence and particle acceleration in supernova remnants

Andrei M. Bykov[*], Sergei M. Osipov[†], and Yury A. Uvarov[‡]

Ioffe Institute, 194021, Saint-Petersburg, Russia

Donald C. Ellison[§]

Physics Department, North Carolina State University, Box 8202, Raleigh, North Carolina 27695, USA

Patrick Slane[‖]

Harvard-Smithsonian Center for Astrophysics, Cambridge, Massachusetts 02138, USA

We show here that highly polarized x-ray synchrotron radiation from young supernova remnants (SNRs) can be modeled within the framework of diffusive shock acceleration (DSA) and nonlinear magnetic turbulence generation. Cosmic ray acceleration by SNR shocks to very high energies requires efficient magnetic turbulence amplification in the shock precursor. As the strong turbulence generated by Bell's instability far upstream from the viscous subshock convects through the subshock, nonlinear dynamical effects on the large amplitude, compressible fluctuations produce a downstream layer filled with strong anisotropic turbulence with predominantly radial magnetic fields. The synchrotron radiation from shock accelerated electrons in the turbulent downstream layer has a high degree of polarization shown to be consistent with recent observations of young SNRs by the *Imaging X-ray Polarimetry Explorer (IXPE)* taking into account high-energy electron losses and line-of-sight integration in a spherical remnant. In the case of our model of Tycho's SNR, the measured x-ray radiation constrains the thickness of the energy containing interval and the amplitude of cosmic ray driven magnetic turbulence, as well as the maximal energy of accelerated protons. The preferential direction of the x-ray polarization depends sensitively on the SNR shock velocity and the ambient density. A fast shock in a region with high enough density is a favorable place to produce tangential polarization of synchrotron radiation, i.e., a dominantly radial magnetic field. A unique feature of our model is the sensitive dependence of the degree and direction of x-ray polarization on the spatial overlap between regions of amplified magnetic turbulence and TeV electron populations. While this overlap occurs on scales orders of magnitude below the resolution of *IXPE*, its polarization measurement allows testing of turbulent plasma processes on unprecedented scales.

I. INTRODUCTION

Radio, x-ray, and gamma-ray observations have proved undoubtedly that young supernova remnants (SNRs) are cosmic ray (CR) accelerators [1–5], while there are still important unresolved questions concerning details of the physical processes involved. Accelerated relativistic electrons emit synchrotron radiation in SNR magnetic fields [6] which is detected in radio and x-rays in young SNRs. High angular resolution *Chandra* observations provided clear evidence for strong, nonadiabatic amplification of magnetic fields in the vicinity of SNR forward shocks [e.g., [1,7]].

Detection and mapping of polarized synchrotron radiation is a powerful observational tool to probe the structure of magnetic fields. This can be performed in the x-ray [see e.g. [8–10]] and radio bands [see e.g. [11,12]]. Radio polarization observations of Tycho [13,14] and a few other young SNRs [15,16], revealed magnetic fields that are predominantly radial at the SNR blast wave rim. The degree of polarization in the limb brightened rims of Tycho reach 20%–30%, while it is about 7% in the main shell observed at a wavelength of 6 cm [13]. The radio polarization in Tycho's SNR shows a relatively high degree of polarization (DP) [17] for which the magnetic field is organized in loose cell-like structures with a maximal scale size of about 110 arcseconds (1.3 pc).

The modern *Imaging X-ray Polarimetry Explorer* (*IXPE*) spacecraft, using photoelectric detection technologies [18,19], recently discovered polarized x-ray radiation from the young SNRs Cas A [20], Tycho [21], and SN1006 [22].

[*]Contact author: byk@astro.ioffe.ru
[†]Contact author: osm.astro@mail.ioffe.ru
[‡]Contact author: uv@astro.ioffe.ru
[§]Contact author: ellison@ncsu.edu
[‖]Contact author: slane@cfa.harvard.edu

With the *IXPE* spatial resolution (~30 arcseconds) it was possible to measure the DP from a few localized sub-parsec scale regions in the Western part of Tycho with the maximal DP of 23% ± 4%. The DP averaged over the whole remnant is 9% ± 2%. Significantly, the direction of the observed polarization is mainly tangential to the shock, a signature of preferentially radial magnetic fields in the x-ray synchrotron emitting region.

The observation of polarized x-ray synchrotron radiation in SNRs indicates the presence of electrons accelerated above TeV energies in amplified, turbulent magnetic fields. The most likely explanation for this electron acceleration is nonlinear diffusive shock acceleration (DSA) driving Bell's instability for the generation of strong magnetic turbulence [see, e.g., [1,23–25]]. At first glance, the high degree of x-ray polarization measured by *IXPE* is difficult to understand since the strong magnetic turbulence required by efficient DSA should limit the polarization. Here, we describe a model that can consistently account for the observed polarization and efficient particle acceleration with nonlinear DSA. We emphasize that the observation of such high polarization is an important clue to the nature of structured turbulent magnetic fields deep inside the remnant, as well as the very high energy particle distribution.

A number of magnetic field amplification mechanisms have been considered for SNRs including, in particular, the Rayleigh Taylor instability [see e.g., [26,27] for a MHD model]. The observation of polarized x-ray emission adds an important constraint on any amplification model by adding information on the morphology of the magnetic field as well as the strength. Here we present a model of polarized x-ray synchrotron emission from Tycho's SNR where CR driven instabilities produce the magnetic turbulence amplification [23–25,28–31].

The bright narrow rims of nonthermal x-ray emission revealed in *Chandra* images in the vicinity of the forward shocks of a few young SNRs is clear evidence for amplification of magnetic fields by a factor of 50–60 or more, well above that expected from MHD processes. Diffusive shock acceleration is the most promising mechanism of CR acceleration in SNRs [e.g., [23,32,33]]. The strong nonlinear nature of DSA, coupled with the generation of large CR currents in the shock precursor, naturally supports Bell's instability for producing magnetic turbulence strong enough to allow SNR shocks to accelerate CRs to well above TeV energies.

II. MODEL DESCRIPTION

In this paper we model the spatial structure of anisotropic magnetic turbulence together with the acceleration of multi-TeV electrons producing synchrotron photons. Our model assumes that thin x-ray filaments observed in young SNRs are synchrotron radiation produced by multi-TeV electrons accelerated by DSA at the remnant forward shock. Models of DSA in young SNRs require a high

level of magnetic turbulence of rather short scales in the shock precursor (gyro-scales of CRs are typically well below 0.1 pc). It has been shown that CR proton driven instabilities [e.g., [23,24,30]] can amplify seed circumstellar magnetic fluctuations to provide this turbulence. Specifically, Bell's nonresonant instability, driven by CR currents in the shock precursor, was shown to provide the required high level of turbulence amplification [25,28,31,34,35]. The turbulence has a slightly smaller longitudinal component of the magnetic field than transverse. Moreover, the nonlinear phase of Bell's turbulence produces strong plasma density fluctuations on CR gyro-scales.

The upstream plasma density fluctuations convect into the viscous subshock and produce shock surface ripples. These ripples in turn efficiently produce turbulence behind the shock [36–41]. The downstream turbulence is anisotropic where the RMS direction of the fluctuations is preferentially longitudinal, i.e., perpendicular to the shock surface [28,42–44].

The physical mechanism we consider for amplification of the downstream magnetic field has three main phases. First, CR protons accelerated by a strong collisionless shock stream into the upstream shock precursor where their current amplifies seed magnetic turbulence by nonlinear CR-driven instabilities [e.g. [25,30]]. We specifically consider the Bell instability generated by the high-energy CR proton current leaving the shock far upstream. The same DSA process accelerates ambient electrons in young SNRs to above TeV energies. Second, the plasma density perturbations produced during the nonlinear evolution of Bell's magnetic turbulence in the CR precursor convect into the viscous subshock and produce ripples in the subshock surface. These ripples (corrugations) efficiently produce intense plasma fluctuations, containing a sizeable fraction of the turbulent energy, that propagate downstream from the subshock [see e.g. [36,37,45,46]]. The shock corrugations may also affect the energetic particle injection process [see e.g. [47]].

Third, as the turbulence convects, it produces intense, anisotropic magnetic turbulence in a layer just behind the shock. The amplification process is the small scale turbulent dynamo mechanism described in [48–51]. Importantly, the character of the magnetic field anisotropy changes with distance downstream. The transverse component (i.e. along the shock surface) of the magnetic field is amplified by the shock compression and it dominates over the longitudinal one in the turbulent field immediately after the shock jump. However, the anisotropic plasma turbulence preferentially amplifies the longitudinal magnetic field component.

Thus, at a distance from the shock on the order of the characteristic scale of the upstream turbulence, the downstream RMS turbulent magnetic field may switch polarities and become dominated by the longitudinal field component resulting in transverse polarized synchrotron radiation from relativistic electrons. We defined here the characteristic scale of the CR driven upstream turbulence at the peak of
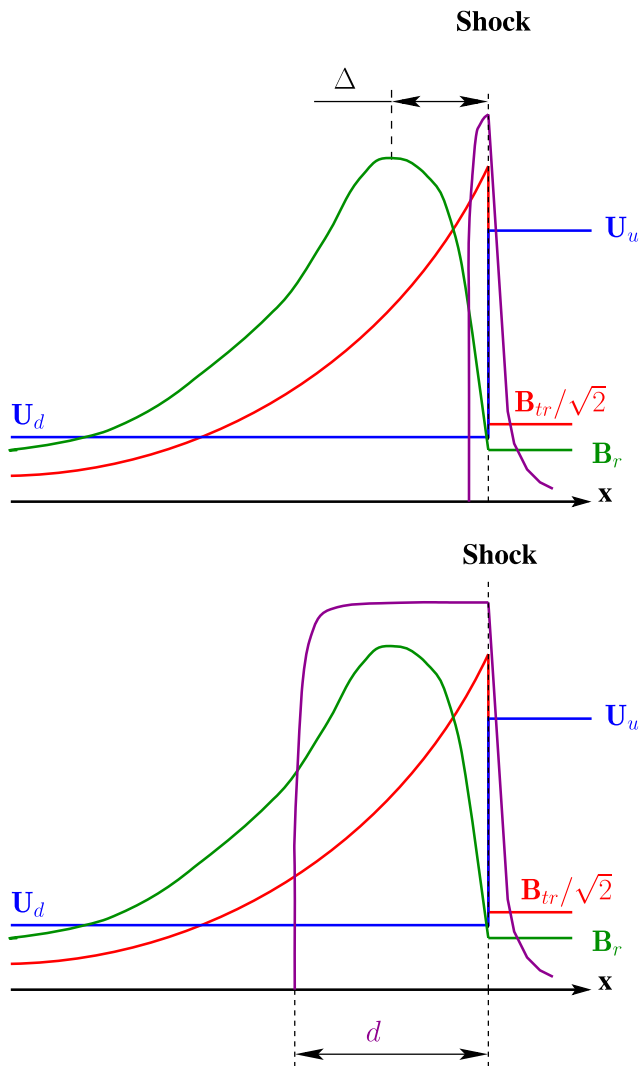
FIG. 1.   In this schematic picture the upstream region is to the right and the shocked, downstream region is to the left. The blue curve shows the plasma flow speed measured in the shock rest frame. The RMS amplitude of the radial magnetic field, B_r, is shown in green, while the transverse magnetic field amplitude B_{tr} (divided by $\sqrt{2}$ as explained in the text) is shown in red. The peak of the transverse field is at the shock as expected from the compression of the transverse component. The turbulent parallel field is amplified by the dynamo mechanism as the plasma flows downstream and the peak is shifted from the shock surface to a distance Δ. The violet curves are electron distributions peaking within a layer of thickness d downstream. x-ray synchrotron emission will peak in regions where both electrons and magnetic field are strong. The upper panel illustrates a case where $d \ll \Delta$ and the x-ray polarization will be predominantly radial. The lower panel illustrates a case where $d > \Delta$ and the x-ray polarization is mainly transverse to the shock normal.

the energy containing interval in Fig. 3. Farther downstream, the dynamo produced magnetic turbulence decays in the absence of driving sources, in accordance with MHD models discussed, e.g., by [52]. The RMS amplitudes of the

longitudinal (green line, B_r) and the transverse (red line, B_{tr}) components of the turbulent magnetic field are shown in Fig. 1.

The strong amplification of the turbulent magnetic field in the shock vicinity increases the synchrotron losses of relativistic electrons. The highest energy electrons, which radiate the x-ray synchrotron photons in young SNRs, are distributed in a narrow layer around the subshock (see for a review [1]), as shown in Fig. 1 by the violet lines. Lower energy radio-emitting electrons would have a broader distribution. The observed direction of x-ray synchrotron polarization depends on the width of the electron distribution together with the amplitude of the turbulent field (green and red curves in Fig. 1). If the high energy electron distribution is wide enough to extend farther behind the shock than the peak of the green line (bottom panel in Fig. 1), the polarization direction will be transverse, as is indeed observed in x-ray observations of Tycho's SNR, and in many radio images of young SNR as mentioned above. If the case with a narrow electron distribution occurs (top panel of Fig. 1), the x-ray polarization will be longitudinal.

To demonstrate our model, we choose parameters typical of Tycho's SNR. Tycho is an extended young remnant for which deep x-ray (*Chandra*) and polarimetric (*IXPE*) observations are available, as well as extensive multi-wavelength data. An analysis of Tycho's expansion rate [53] derived the maximum forward shock velocity of ~5300 km s^{-1}, assuming the distance to Tycho to be 2.3–4 kpc.

Indications of order-of-magnitude variations in the ambient density around the periphery of Tycho's forward shock, possibly due to interactions with dense clumps of the interstellar medium, were found by [54]. While the mean ambient number density is about 0.1–0.2 cm^{-3}, they found that in the Western regions it may be 3–10 times higher compared to that in the southwest (see also [55–57] for recent discussions). The map of polarized x-ray emission of Tycho's SNR by [21] revealed a high degree of polarization in the northeast region. To model synchrotron x-ray radiation from different regions we consider a range of ambient number densities below 1 cm^{-3}.

III. INTENSITY AND POLARIZATION SIMULATION

The intensity and polarization of Tycho's synchrotron map can be obtained after integration of the Stokes emission parameters over the line-of-sight (LOS) using formulas for synchrotron radiation obtained in [6]. The details are in Appendix A. Briefly: as the plasma flows downstream from the subshock, the evolution of the turbulent magnetic field and the electron distribution function are calculated. The strong synchrotron losses produce a spatial inhomogeneity where the radiation is concentrated in a thin layer just downstream from the subshock. However, general formulas have been simplified

using some assumptions of the problem symmetry and averaging.

The magnetic field simulation is discussed in Sec. IV. The field was calculated for a plain shock geometry in a cubic box of size $\sim 10^{17}$ cm (see Sec. IV). Since the Tycho SNR radius is $\sim 10^{19}$ cm, larger than our box size, we must extrapolate and adjust for the spherical remnant to calculate the polarization degree and emission radial profile across the remnant.

First of all, we construct smooth analytical approximations for square-averaged magnetic fields neglecting small scale fluctuations, as described in Appendix B. The approximation has a different functional dependence on distance from the shock for radial (B_r) and transverse (B_{tr}) field components. B_r is directed along the SNR radius while B_{tr} is normal to B_r. We assume spherical symmetry and local axial symmetry of an anisotropic magnetic field where the direction of B_r is the axis of symmetry. While integrating along the LOS we average over the transverse magnetic field direction (and over small scale magnetic fluctuations, see Appendix A) at each local point.

Diffusive shock acceleration produces an approximate power law distribution of high energy electrons in a broad energy band with an exponential cut off at some energy. However, the synchrotron x-ray photons observed in the 1–8 keV range were emitted by electrons in a narrow energy interval above 1 TeV. Therefore, even in the cut-off regime, one can approximate the electron distribution function for the observed radiation as a power law $f_e(E) = K_e E^{-p}$. In this case the integration over energy can be done analytically and the local averaging over stochastic magnetic fields described in Appendix A can be done after it. After integration along the LOS a 1-dimensional SNR intensity and polarization degree radial profile can be obtained.

Because of the strong synchrotron losses from the magnetic field jump at the subshock, x-ray emitting electrons are located in a thin layer near the subshock. As a result, the x-ray emission of synchrotron photons of frequency ν is also located in a thin layer of width $d(\nu)$. The dependence of this depth, d, on photon frequency, i.e., $d \propto 1/\sqrt{\nu}$, was obtained in a homogeneous magnetic field model in [1], where different transport regimes of electrons in the emitting layer were discussed. We generalized this relation for an inhomogeneous magnetic field decreasing in the downstream direction and calculated $d(\nu)$ numerically. We find for our model magnetic field in the x-ray frequency range that $d \propto 1/\nu^I$, where $I \approx 0.5$–1.0 (depending on L_0, the correlation scale of the initial seed magnetic fluctuations).

For a homogeneous field ($d \propto 1/\sqrt{\nu}$) the observable synchrotron spectrum integrated over the LOS (or over the emission volume) has an index that is greater by $1/2$ than that for the local emission spectrum. In this case, the electron spectral index obtained from the emission spectrum observed from the total emission volume $p_{obs} = p + 1$. For the
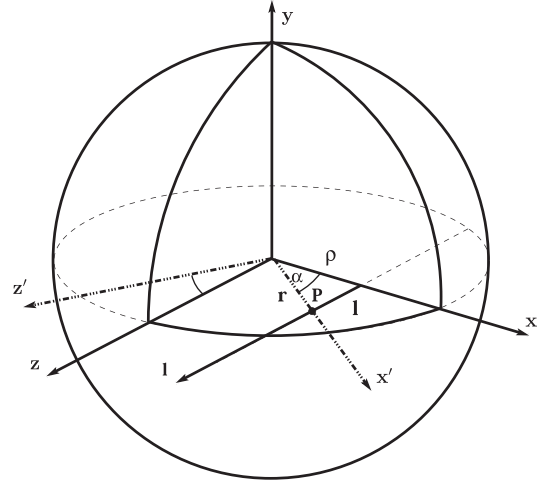

FIG. 2. Spherical approximation for Tycho's SNR. The z-axis and the LOS l are directed to the observer. The x-axis is chosen so the LOS is lying in the x, z plane. The x'-axis, that crosses the LOS at the point P, is inclined to the x-axis at an angle α. (ρ, l) are the (x, z) coordinates of the point P, and r is its distance to the center of the remnant.

simulated inhomogeneous magnetic field (discussed in Sec. IV) $d \propto 1/\nu^I$ and $p_{obs} = p + 2I$. The position of the peak of the radial magnetic field component generated near the shock is shifted by a distance Δ toward the center of the remnant from the position of the peak of the tangential field component (see Fig. 1).

A polarization direction and degree of the x-ray synchrotron emission from the SNR ridge is defined by the proportion of the magnetic field projections B_y and B_x to the plane transverse to the LOS (see Fig. 2 and Appendix A). If the stochastic magnetic field dominates over the mean field, $B_y = B_{tr}/\sqrt{2}$. For points along the LOS with $\alpha = 0$ (Fig. 2), $B_x = B_r$. The components B_r and $B_{tr}/\sqrt{2}$ are plotted in Figs. 1 and 5.

If the depth of the x-ray emitting layer $d \lesssim \Delta$ (bottom panel of Fig. 1), the total magnetic field can be considered almost constant over a length d and the relation $p_{obs} = p + 1$ approximately holds. If $d \ll \Delta$ (top panel of Fig. 1) the tangential magnetic field dominates and radially polarized emission is expected. As the width of the electron distribution d increases toward the remnant center, the radial magnetic field contribution increases so the polarization degree decreases at first up to some width $d \sim \Delta$. For wider electron distributions $d \gtrsim \Delta$, the radial magnetic field dominates and the polarization increases in the tangential direction. This scenario works if the radial magnetic field amplification in the downstream is sufficient.

The value of the photon spectral index found in [58] for the near ridge regions of Tycho's SNR lies in the interval 2.5–3.2. The corresponding electron indexes $p_{obs} \approx 4.0$–5.4 and the allowed local range is $p \approx 2.0$–4.4. The local value $p = 3.0$ is used in our simulations. The uncertainty in p leads to
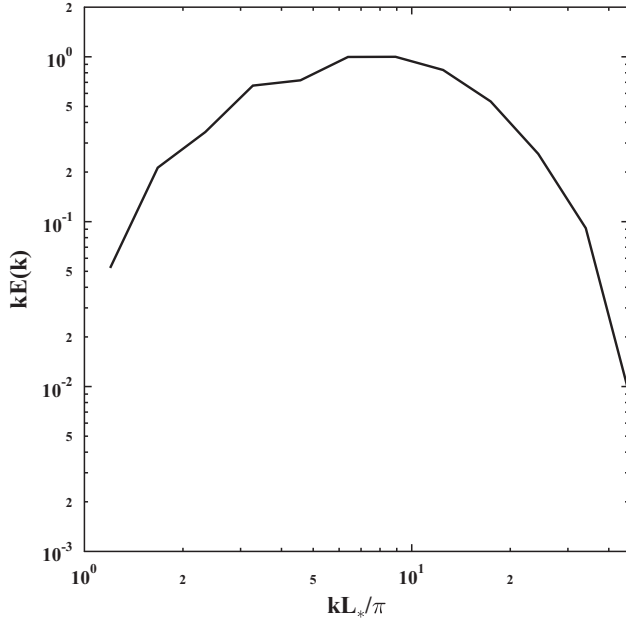
FIG. 3. Magnetic field energy spectrum normalized to the maximum of the curve at the end of the setup simulation for magnetic field amplification by the CR driven instability in the shock precursor. As it is seen the energy containing scale of the turbulence is $\sim L_*/3$ in this case.

$\sim 15\%$ error in the polarization degree calculation which is less than the observational error given in [21].

IV. SETUP

In this section, we describe the numerical ideal MHD modeling, that uses the open code PLUTO [59] to obtain radial profiles of the magnetic field near the shock necessary for calculating synchrotron radiation. We create dimensionless parameters using the following normalizations: $\rho_* = 1.67 \times 10^{-24}$ g/cm^3 for number density (i.e., 1 proton per cm^3), $L_* = 5 \times 10^{16}$ cm for length, and $u_* = 10^8$ cm/s for speed. The calculations use the ROE solver, parabolic reconstruction, the third-order Runge-Kutta scheme for time steps, and the Eight-Wave Formulation to control the zero divergence of the magnetic field ($\nabla \cdot \mathbf{B} = 0$).

The MHD simulation procedure has two distinct stages. In the first stage, we fix an external cosmic ray current in a box filled with ambient plasma. This 3D simulation runs for a time corresponding to the time needed for a plasma parcel to cross the precursor of the shock. During this time, Bell's turbulence with magnetic field and density fluctuations is generated. Both the CR current and the scale size of the shock precursor are consistent with the values obtained in our nonlinear, kinetic Monte Carlo model of shock acceleration in Tycho's SNR [31]. After a shock precursor crossing time, we freeze the turbulence amplified by Bell's mechanism in the box. The plasma in this first simulation is

then used as a boundary condition for the MHD shock simulation.

Bell's instability occurs in the shock precursor and is driven by the electric current $\mathbf{j}^{cr}$ of accelerated protons, as measured in the upstream plasma rest frame [25,28,60]. Large hybrid simulations of magnetic turbulence amplification in DSA [35] demonstrated that Bell's instability grows faster than the resonant instability in shocks with Alfvenic Mach numbers larger than 30. This is the case for the forward shock in Tycho's SNR.

The equation of motion of a perturbed background plasma in the same frame can be written as

$$\rho\left(\frac{\partial \mathbf{u}}{\partial t} + (\mathbf{u}\nabla)\mathbf{u}\right) = -\nabla p + \frac{1}{4\pi}(\nabla \times \mathbf{B}) \times \mathbf{B} - \frac{1}{c}(\mathbf{j}^{cr} \times \mathbf{B}),$$
(1)

where ρ is the plasma density, $\mathbf{u}$ is the plasma velocity, $\mathbf{B}$ is the magnetic field, p is the pressure, and c is the speed of light.

To initiate Bell's instability, the CR current $\mathbf{j}^{cr}$ can be considered constant [see e.g. [25,28]] given the small response of the CR current to the short wavelength unstable fluctuations. Then, Eq. (1) differs from the adiabatic, single-fluid MHD equations solved by the PLUTO code only by an external force term. We introduced an external force term driven by the CR current into the momentum and energy balance equations. For the initial Bell instability calculation we use a cubic box containing $64 \times 64 \times 64$ cells. Our downstream magnetic field MHD simulation (second stage) and polarization calculations use a box with $2560 \times 512 \times 512$ cells.

The coordinates for the setup box, normalized to L_*, range from -1 to 1 along each side of the box. Periodic boundary conditions are set at all box boundaries. The code is initiated at $t = 0$ with the velocity $\mathbf{u} = 0$ and $\rho/\rho_* = 0.3$. The same ambient density was used by [61] in a non-equilibrium model of broadband emission from Tycho's SNR. Our simulation is done in the upstream plasma rest frame. Note that there is no shock in the calculation of Bell's instability. The CR proton electric current is directed opposite to the x-axis such that $j_x^{cr}/j_* = -4$, $j_y^{cr}/j_* = 0$, and $j_z^{cr}/j_* = 0$, where the normalization electric current is

$$j_* = \frac{c\sqrt{\rho_*}u_*}{L_*\sqrt{4\pi}}.$$
(2)

The initial magnetic field consists of a constant component directed along the x-axis equal to $B = 3$ μG, and a seed turbulent component represented by the sum of modes with a RMS value of $\delta B_{\mathrm{rms}} = 0.1B$, where

$$\delta\mathbf{B} = \sum_n a_n \mathbf{e}_n \cos(\mathbf{k}_n\mathbf{r} + \Psi_n).$$
(3)

Here $\mathbf{k}_n$ is a mode wave number, $a_n \sim k^{-11/6}$ is a mode amplitude (the wave number dependence corresponds to Kolmogorov turbulence), $\mathbf{e}_n$ is a unit mode polarization vector, and Ψ_n is a mode phase (random). The components of the mode wave numbers are

$$k_{nx} = \frac{2\pi i}{L}, \qquad i = 0, 1, 2, \ldots 9, \qquad (4)$$

$$k_{ny} = \frac{2\pi j}{L}, \qquad i = 0, 1, 2, \ldots 9, \qquad (5)$$

$$k_{nz} = \frac{2\pi k}{L}, \qquad i = 0, 1, 2, \ldots 9, \qquad (6)$$

where L is the length of the box edge (in these simulations $L/L_* = 2$), and the sign of the wave vector component is chosen randomly. The vector $\mathbf{e}_n$ is chosen randomly in the plane perpendicular to $\mathbf{k}_n$.

In order to setup the amplified magnetic turbulence in the simulation box, the simulation is started with initial seed fluctuations and run long enough for an upstream plasma parcel to cross the shock precursor. In physical units for Tycho's SNR, this time is about 20 yrs, i.e., the time for plasma to flow with the shock speed the distance of ~0.1 pc between the free escape boundary and the viscous shock [see, e.g., [31]]. During this time, the CR current will amplify the background turbulence via Bell's instability.

At the end of the simulation the RMS magnetic field was $B_{\rm rms} \approx 94$ μG. The ratio of the RMS turbulent density to the average density was ≈0.39. In Fig. 3 we show the magnetic field energy spectrum normalized to the maximum of the curve at the end of the CR driven turbulence simulation. It can be seen from Fig. 3 that the turbulence characteristic scale L_0 is $kL_*/\pi \approx 6$, that is $L_0 = 2\pi/k \approx L_*/3$, where L_0

is of the order of the gyroradius of a CR proton of maximal energy (derived in the amplified field).

The second stage of the calculation is performed using the results of the first stage simulation as a boundary condition on the left side of the simulation box. This simulation is done in the shock rest frame. The main simulation box has dimensions of $2560 \times 512 \times 512$ cells, the plasma flows along the positive x-axis, and all coordinates are normalized to L_*. The x-axis ranges from 0 to 10 over 2560 cells and the perpendicular y- and z-axes range from −1 to 1 (as in the previous setup calculation). Periodic boundary conditions are set for the sides of the box that are parallel to the x-axis. An outflow boundary condition is set on the downstream side of the box at $x/L_* = 10$. A 4000 km s⁻¹ shock is initiated in the simulation box. Plasma flows from left to right across the left boundary x = 0 at a speed of 4×10^8 cm/s, and the plasma crossing the left boundary is the turbulent plasma from the first simulation stage (similar to what was done in the paper [28]).

Since the time for plasma to convect to the downstream wall of the second stage simulation box is greater than the size of the simulation domain of the first stage divided by the upstream speed, we use a cycling procedure where we repeat the injection of the Bell turbulent plasma as often as necessary. The transformation of the first stage simulation data to the shock rest frame is taken into account. The interpolation of the data obtained at the first stage into the cells of the left boundary of the main box is performed using methods built into PLUTO. The accelerated proton current is set to zero so Bell's instability is inactive. The box extension in the x-direction is determined by the grid resolution and calculation time.

The shock initiation was done as follows. At the initial moment of time, at the point $x/L_* = 2$, a shock is set: for
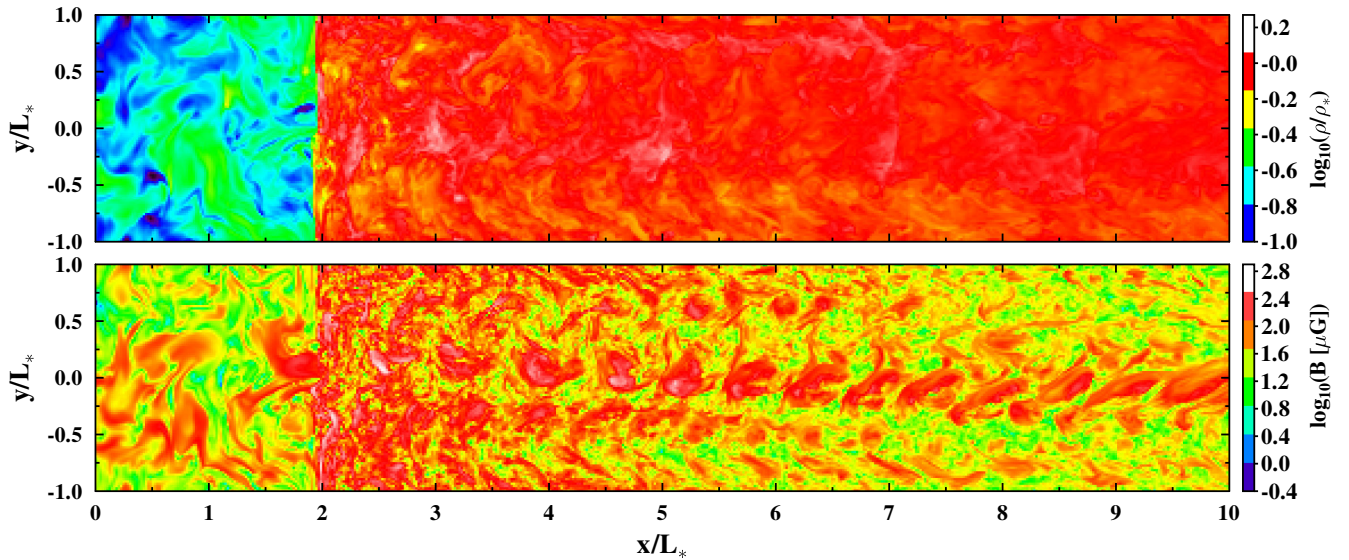

FIG. 4. Spatial slice of the plasma density (top panel) and the magnetic field modulus (bottom panel) at the end of the simulation for $z = 0$.
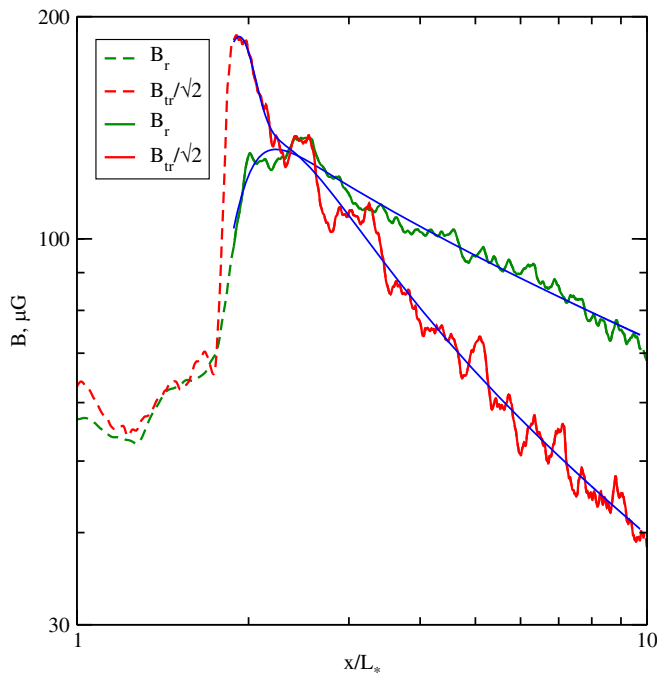
FIG. 5. This figure shows the magnetic field projections B_r (green) and B_{tr} (red) mean-square averaged over the simulation box slices with fixed x-coordinates (in our model the r and x-coordinates are identical). The analytical approximations fitting the simulation data are shown in blue. The fitting is only done over the region shown with solid curves.

$x/L_* < 2$, the flow velocity equal to 4×10^8 cm/s is directed along the x-axis, the density is equal to the average value from the setup simulation, the magnetic field is directed along the x-axis and is equal to 3 μG, and the pressure is equal to the average pressure in the box of the first stage calculation. With these values, the shock has a Mach number $M \approx 4$. At $x/L_* \geq 2$ all values are determined from the Rankine-Hugoniot conditions, so the shock remains almost at rest in the box frame.

Figure 4 illustrates the spatial distribution of the plasma density and the magnetic field in the computational domain at the end of the simulation. The RMS magnetic field simulation results are shown in Fig. 5. This mean-square averaging was done over the (y, z) plane for each x coordinate. The red curves are the transverse components B_{tr}, the green curves are the longitudinal components B_r, and the blue curves are fitted analytic approximations. As expected, the transverse components show a sharp increase from the density compression as the plasma crosses the subshock at $x \approx 2L_*$. As the plasma continues to flow downstream B_{tr} decreases.

In contrast, the longitudinal component B_r shows a modest increase immediately at the shock but is enhanced by the small-scale dynamo mechanism as the plasma flows downstream. At some distance downstream, B_r becomes, and remains, substantially greater than B_{tr}.
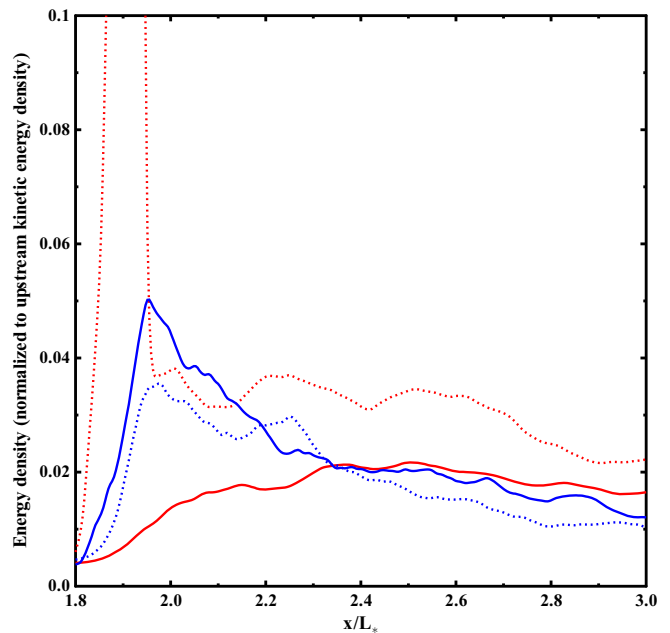

FIG. 6. Energy density of downstream turbulence normalized to the far upstream kinetic energy density. The dotted curves show kinetic energy densities derived from plasma motions while the solid curves show magnetic field values. The large peak in the radial component of radial velocity fluctuations (red dotted curve) comes from the corrugation of the shock surface since the averaging was done over slices of constant x which intersect both upstream and downstream flows with significantly different speeds. The width of the peak is about the energy containing scale of the upstream turbulence (see Fig. 3). The strong shock corrugations drive the radial anisotropy of the downstream turbulence. The radial magnetic field component is the solid red curve while the transverse field component is the solid blue curve. The growth of the radial magnetic component and its dominance over the transverse component with distance is seen.

A unique feature of our model, stemming from the delayed dynamo effect, is the spatial inhomogeneity in polarization direction. This is shown in Fig. 6. The longitudinal magnetic field component is weaker than the transverse component immediately behind the shock but experiences growth from the dynamo effect as the plasma convects away from the shock. At some point downstream, depending on the SNR parameters, the longitudinal component may dominate in the main part of the emitting volume. Our model connects the SNR parameters (e.g., shock speed, ambient density) to polarization direction, as well as giving a rationale for how anisotropic turbulence can coexist with efficient DSA.

V. SIMULATIONS VS OBSERVATIONS

We compare our simulation results for Tycho's SNR to *Chandra's* x-ray radial intensity profiles obtained for the 4–6 keV energy range [58], and *IXPE's* x-ray polarization maps obtained for the 3–6 keV energy range [21].

The *Chandra* data has near arcsec angular resolution for the 4–6 keV energy band and is free of emission lines. *IXPE* has much lower angular resolution. We convolved our simulation results with the *Chandra* and *IXPE* point-spread-functions (PSFs), using the model of [62] for *IXPE*. For our comparison, we assume a photon energy of 3 keV and the synchrotron fraction in the total emission equal to be 0.6 for Tycho SNR (see [10]). The polarized photon fraction for other young SNRs remnants may be either larger, if the shock is propagating in rarefied plasma (e.g. in a progenitor star wind), or smaller in the case of SNR shells with bright unpolarized thermal emission. Therefore, the polarization degree estimation for these SNRs would differ from the case of Tycho's SNR discussed in the paper.

The *Chandra* PSF was simulated using the psfFrac function in Python's psf module [63] for 4 keV photon energy and an offset of 4 arcmin (i.e., the Tycho SNR ridge offset in the *Chandra* observations used by [58]). For *Chandra*, 80% of the point source emission at 4 keV is concentrated in a circle of ~0.7 arcsec radius for the on-axis direction, and in a circle of ~2.3 arcsec radius for the

4 arcmin off-axis direction. Magnetic field samples used in the simulation are discussed in Sec. IV.

If the depth of the x-ray emitting layer $d \ll \Delta$, the magnetic field in the emitting layer is tangent to the shock front and the synchrotron emission is polarized radially. In the opposite case $d \gtrsim \Delta$, the magnetic field is radial in most of the emission layer and the polarization of the total synchrotron radiation is tangential. In the intermediate case the polarization degree of the total emission should be low because of the near equal intensity of radial and transverse emission. This is illustrated in the lower panel of Fig. 7 with the $L_0 = 3 \times 10^{15}$ cm example ($\Delta \propto L_0$).

It should be mentioned that the *IXPE* ~30 arcsec PSF radius is greater than the angular value of Δ (Fig. 1) so *IXPE* measures the intensity and polarization from the total emission layer. [21] found that there is a rather high tangential x-ray polarization emission from the ridge of Tycho. The polarization degree is ~20% from the north-west ridge region and ~10% overall (while estimated errors are rather high). We conclude from this that $d \gtrsim \Delta$ for Tycho. Our simulation results show that if the polarization is transverse and high ($\geq 10\%$), the value of L_0 is limited from the upper side, i.e. $L_0 \lesssim 2 \times 10^{15}$ cm (Fig. 7).

Figure 8 shows the x-ray intensity profile after convolution with the *Chandra* PSF. The data points in green are from [58]. Our results are sensitive to the value of d. If $d \gg \Delta$, the x-ray *Chandra* intensity profile near the ridge is determined by the asymptotically falling downstream magnetic field (see Fig. 5 and Appendix B) and is too broad for a good fit to the data. However, a high transverse *IXPE* polarization in our model demands that $d \gtrsim \Delta$. This case is shown in the bottom panel of the Fig. 1.
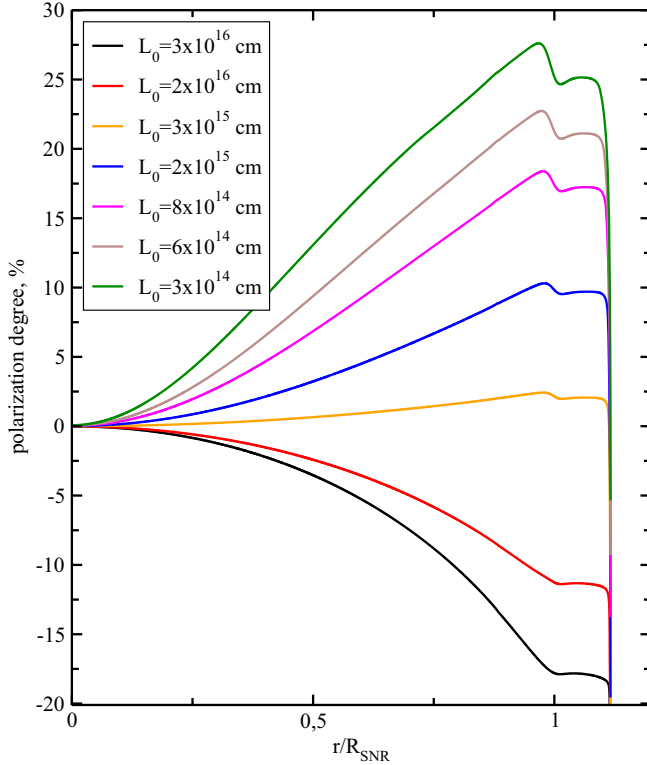

FIG. 7. X-ray polarization percentages as a function of position downstream from the shock for different model magnetic field profiles. The polarization for different values of L_0 is obtained by convoluting the *IXPE* PSF for 3 keV photons for different values of L_0. The polarized synchrotron photon fraction was assumed to be 0.6, as was estimated earlier for Tycho's SNR (see the text). Positive and negative values indicate transverse and radial directions of polarization respectively.
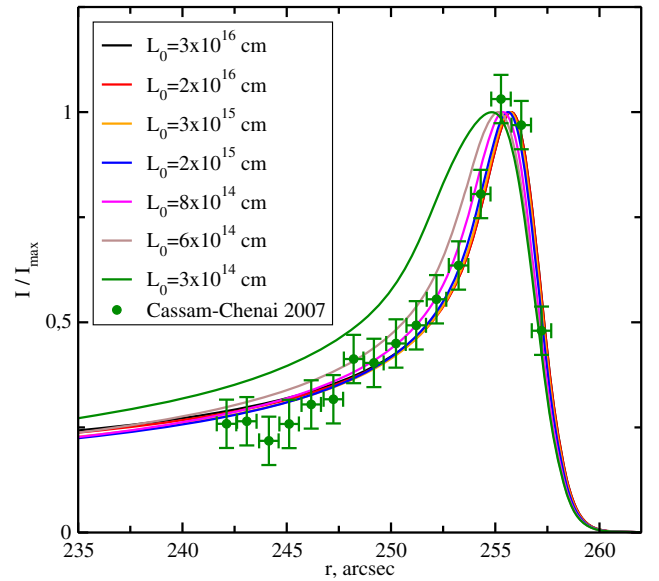

FIG. 8. Simulated *Chandra* intensity profiles after convolution with the *Chandra* PSF for 4 keV photons for different values of L_0. The data points obtained in [58] are shown in green.

With decreasing L_0 (L_*) the depth of the layer with high magnetic field ($\sim\Delta$) decreases as does the gross synchrotron losses in the shock vicinity. Because of the lower loss rate, the width d of the layer of x-ray emitting electrons increases. If d is less than or equal to the *Chandra* PSF radius, the profile width is defined by the latter and is almost independent of d. This is the reason why in Fig. 8 there is almost no dependence on L_0 if the turbulent scale $L_0 \geq 8 \times 10^{14}$ cm.

For a Tycho SNR distance of 2.5 kpc, 1 arcsec is $\sim 4 \times 10^{16}$ cm. The *Chandra* PSF radius at the ridge is ~ 2.5 arcsec so an upper value for d below which the intensity profile only weakly depends on d is $\sim 10^{17}$ cm. For the x-ray intensity profiles shown in Fig. 8, only the $L_0 = 3 \times 10^{14}$ cm case has $d \approx 1.6 \times 10^{17}$ cm that exceeds the *Chandra* PSF radius. The $L_0 = 6 \times 10^{14}$ cm case has d that is approximately equal to it and for all the other plotted curves d is lower. Figure 8 shows that the data points of [58] are well fitted if $d \lesssim \text{PSF}_{\text{Chandra}}$ and the fit quality worsens if this condition breaks. This allows an estimate of the width of the emission layer to be $d \lesssim \text{PSF}_{\text{Chandra}}$. If besides a good fit of the intensity profile we need a high transverse polarization, then $\Delta \lesssim d$ holds so Δ is also less than the *Chandra* PSF radius.

While the shock propagates in the turbulent medium its front should be perturbed. This effect should increase the observable ridge width after projection over the LOS and averaging. Such averaging is used in the Chandra data processing when counts are gathered from a rather broad sector of the SNR image to obtain 1-dimension radial profile [58]. Thus the condition $d \lesssim PSF_{\text{Chandra}}$ also limits the front ripple amplitude.

VI. DISCUSSION

Radio and x-ray observations of young SNRs have revealed in a few cases polarized synchrotron radiation produced by predominantly radial magnetic fields. Magnetic turbulence with predominantly radial anisotropy can be produced under certain conditions in the downstream of a strong shock propagating in a turbulent medium (see, e.g., [28,42,43]). We have described here a physical mechanism for producing strong turbulence with predominantly radial anisotropy downstream from a SNR shock undergoing efficient DSA and producing high energy CRs. We show how strong fluctuations with predominantly radial direction are amplified by the anisotropic turbulent plasma motions.

The anisotropic plasma velocity fluctuations behind the shock are produced by upstream density fluctuations flowing into the subshock. These density fluctuations are generated in the shock precursor by the nonlinear phase of Bell's instability driven by the electric current of the highest energy CR protons as they escape the accelerator. In our results, density fluctuations of amplitude $\delta\rho/\rho \sim 0.4$ of

scale $L_0 \leq 10^{16}$ cm were produced. As they flow through the subshock, the density fluctuations produce a rippled structure that generates anisotropic turbulence. The RMS magnitude of the parallel field component amplified by the small-scale dynamo mechanism reaches a peak at a distance $\sim L_0$ behind the shock. The turbulence then decays, as shown in Fig. 5.

In principle, the density fluctuations needed to produce the parallel anisotropy of magnetic turbulence could be interstellar or circumstellar turbulence [42,43]. However, the amplitude of density fluctuations of scales $\sim 10^{16}$ cm for normal interstellar turbulence associated with SNRs is expected to be rather small with $\delta\rho/\rho \sim 0.03$.

The degree of x-ray transverse polarization in the western part of Tycho's SNR, as measured by *IXPE* [21], is just above 20%. As shown in Fig. 7, our simulation results can reproduce this high polarization level if the characteristic turbulent scale $L_0 < 10^{15}$ cm. Our model assumes strong magnetic field amplification (well above that due to plasma compression) in the shock precursor in order to match the x-ray profile measured by the *Chandra* observatory with arcsecond resolution [see, e.g., [1,58]]. Cosmic ray driven instabilities [see e.g. [30]] can provide the high amplification of seed magnetic fluctuations in the shock precursor as the CR electric current, J_{CR}, from shock accelerated protons drives Bell's fast nonresonant instability [25]. The wave number of the magnetic fluctuations with the fastest growth rate in Bell's linear theory is $\sim k_0/2$, where the characteristic wave number of the instability is $k_0 = 4\pi J_{CR}/cB$ [25]. Then, the wavelength of the fastest growing fluctuation is $l_0 = cB/J_{CR}$.

In the nonlinear Monte Carlo model of CR acceleration by a strong shock, the accelerated CR protons of maximal energy leave the accelerator at the upstream free escape boundary where the magnetic field magnitude, in the case of Type Ia SNRs, likely corresponds to the interstellar value of a few micro Gauss. Assuming that the characteristic length scale $L_0 \sim l_0$ at the free escape boundary, we can estimate the electric current of maximal energy CRs leaving the accelerator needed to match the polarization observations. This current is $J_{CR} \sim 10^{-10}$ CGSE units and is in good agreement with the free escape boundary current obtained in the Monte Carlo modeling of DSA [31] (see their Fig. 2), where the model shock parameters closely resembled those of Tycho's SNR. The maximal energies of the accelerated protons in the model were well above 10 TeV.

The main result of our modeling of Tycho's SNR is that, by combining the superb angular resolution of *Chandra* data with the x-ray polarization measured by *IXPE*, we are able to probe deep into the CR driven magnetic turbulence on scales smaller than the resolution of either telescope. For example, we show that a transverse polarization of 20%, as measured by *IXPE* in the western part of Tycho's SNR, indicates turbulent scales of $L_0 \lesssim 8 \times 10^{14}$ cm. The intensity profiles measured with *Chandra*'s resolution are consistent

with our model turbulent lengths $L_0 \gtrsim 4 \times 10^{14}$ cm. Despite that the derived length L_0 is less than what can be directly resolved by *Chandra*, the polarization data combined with the model allows a look at scales smaller than the instrument resolution.

The physical reason for this is the overlapping of the narrow layer of very high energy electrons accelerated by DSA (thickness d) with the layer of thickness Δ filled with magnetic fluctuations of predominantly radial direction, as shown in Fig. 1. The thickness d decreases with the magnitude of the amplified magnetic field. The thickness Δ depends on the density fluctuations $\delta\rho/\rho$ just upstream from the shock surface.

It should be noted that while here we concentrated on Tycho's SNR, our model should apply equally well to another young SNR SN 1006. *IXPE* detected a high average x-ray polarization of $\sim 20\%$ with a nearly parallel magnetic field direction in the north-eastern part of SN 1006 [22]. The outer shock of SN 1006 has an estimated shock velocity $\sim 5,000$ km s^{-1} but the ambient density is a few times below what we assumed for Tycho. Despite this difference, the model discussed above can explain the x-ray observations of SN 1006.

The maximum amplitude of density fluctuations in the shock precursor is governed by the saturation level of magnetic turbulence in Bell's instability. For shock velocities $u_s \lesssim 5,000$ km s^{-1}, this is $\propto \rho_0 u_s^3$ (see [25] and Fig. 11 in [31]). Our simulations indicate that Δ is shortened with the growth of $\delta\rho/\rho$ so the fastest shocks with the strongest Bell instability would have a short distance Δ. A short Δ means the radial magnetic turbulence would be concentrated near the subshock and dominate over B_{tr} there. Since the peak amplitude of the radial magnetic turbulence approaches the amplitude of the velocity of radial turbulence, which dominates the energy density in the downstream region (see Fig. 6), the overall polarization in fast shocks will be transverse. On the other hand, slower shocks in less dense regions, e.g., in some regions of RX J1713.7-3946, can be expected to show dominantly transverse magnetic fields in x-ray polarization.

The degree of x-ray polarization measured by *IXPE* from the shells of Cas A, Tycho, and SN 1006 varies from a few percent in Cas A to $\geq 20\%$ in SN 1006 and Tycho. In all three SNRs, the magnetic field direction is predominantly radial. The ratio of the polarized synchrotron emission to unpolarized emission fluxes from the hot thermal gas affects the polarization degree. In fast forward shocks of young SNRs propagating in rarefied plasma the contribution of unpolarized thermal x-ray emission may be small and the synchrotron fraction may exceed 0.6, which we estimated for Tycho's SNR. Then the degree of polarization can substantially exceed $\sim 25\%$ which we derived in Fig. 7 for Tycho's SNR. On the other hand, dense ambient matter may reduce the x-ray polarization degree.

It should be noted that we limit ourselves here to MHD modeling of Bell's instability initiated by a fixed CR current approximation. The CR current in our model mimics the high energy CRs escaping the acceleration region from far upstream of the shock. Particle in cell [64] or kinetic treatments [65,66] can account for the CR current response and nonlinear saturation effects within the accelerator. Presently, the computer resources needed to simulate the multi-scale structure of the extended shock precursor and the evolution of magnetic turbulence in the downstream region, effects important for the problem of interest, are not feasible with the microscopic particle-in-cell technique.

However, magnetic field amplification by CR driven instabilities can be studied with nonlinear kinetic Monte Carlo model (see, e.g., [31]), which use a simplified description of MHD turbulence but account for energy-momentum conservation including the CR current response effects in DSA. The level of magnetic turbulence at the end of the upstream of the fast Tycho's shock dominated by Bell's instability derived in the Monte Carlo simulations is consistent with the turbulent magnetic field magnitude obtained in MHD model described above. This is because the effect of the CR current response is modest in fast shocks with efficient acceleration of protons escaping the accelerator.

Despite these limitations, an important prediction of our results is the dependence of the polarization direction on shock speed. MHD [25] and Monte Carlo models [31]) have shown that the strength of the CR driven Bell instability is higher for faster shocks. We expect fast SNR shocks will have a high degree of transverse polarization. Slower shocks in SNRs in more rarefied plasma can be expected to show dominantly parallel synchrotron polarization as it is observed in radio observations of a number of SNRs [15].

VII. CONCLUSIONS

We show here that the polarized x-ray radiation detected by the *IXPE* telescope from Tycho's SNR can be modeled as the synchrotron radiation of multi-TeV electrons accelerated by diffusive shock acceleration with magnetic field amplification at the fast forward SNR shock. The model determines the degree of polarization and its direction, which corresponds to predominantly radial magnetic fields, consistent with observations.

The nonresonant CR current driven instability [25] amplifies short scale magnetic fluctuations which produce strong density fluctuations in the shock precursor. The interaction of these density fluctuations with the thin collisionless viscous subshock generates intense turbulence immediately downstream from the shock. As the turbulence decays downstream it amplifies magnetic fluctuations producing a radial dominated anisotropy in fast shocks.

Strong magnetic turbulence in the shock precursor is required for DSA to accelerate particles to well above 10 TeV. Our model shows how high polarization levels can be consistent with strong turbulence. The thin synchrotron

filaments detected by *Chandra* are quantitatively explained in the model.

The combined use of *Chandra* and *IXPE* data allows constraints to be placed on properties of magnetic turbulence at scales well below the available resolution of modern high energy telescopes. Future imaging of young SNRs with the high sensitivity at subarcsecond resolution to be provided with the *Lynx* telescope [67] should lead to a fuller understanding of these CR accelerators including the twinkling nature of radiation seen from the shock precursor.

ACKNOWLEDGMENTS

APPENDIX A: EXPRESSIONS FOR SYNCHROTRON POLARIZATION

Intensity and polarization of the Tycho synchrotron map can be obtained after integration of Stokes emission parameters over the LOS using formulas for synchrotron radiation obtained in [6]

$$I(\nu) = \frac{\sqrt{3}e^3}{mc^2} \int dl dE \frac{\nu}{\nu_c} B_\perp(\mathbf{r}) f_e(E, \mathbf{r}) \int_{\nu/\nu_c}^\infty K_{5/3}(\eta) d\eta$$

$$Q(\nu) = \frac{\sqrt{3}e^3}{mc^2} \int dl dE \frac{\nu}{\nu_c} B_\perp(\mathbf{r}) f_e(E, \mathbf{r}) K_{2/3}\left(\frac{\nu}{\nu_c}\right) \cos(2\chi)$$

$$U(\nu) = \frac{\sqrt{3}e^3}{mc^2} \int dl dE \frac{\nu}{\nu_c} B_\perp(\mathbf{r}) f_e(E, \mathbf{r}) K_{2/3}\left(\frac{\nu}{\nu_c}\right) \sin(2\chi) \qquad \text{(A1)}$$

where $\nu_c = 3eB_\perp \gamma^2/4\pi mc$, $\int dE d\Omega_E \cdot f_e(E, \mathbf{r}) = 4\pi \int dE \cdot f_e(E, \mathbf{r}) = n(\mathbf{r})$. I, Q, and $U(\nu)$ are normalized so the radiation flux near Earth is given by $dF(\nu) = I(\nu)d\Omega = (dS/r^2)I(\nu)$ and so on. The function f_e is an isotropic electron distribution function, $\mathbf{B}_\perp$ is a magnetic field projection to a plane transverse to the LOS, and χ is the angle between the fixed direction in this plane and the main axis of the polarization ellipse. The parameters ν_c and χ are functions of $\mathbf{r}$.

Assuming a power law approximation for the electron distribution function, the integration over electron energy can be done analytically, see [6]

$$\tilde{I}(\mathbf{r}, \nu) = W_0 \frac{p + 7/3}{p + 1} B_\perp^{(p+1)/2} \nu^{-(p-1)/2}$$

$$\tilde{Q}(\mathbf{r}, \nu) = W_0 \cos(2\chi) B_\perp^{(p+1)/2} \nu^{-(p-1)/2}$$

$$W_0 = \frac{\sqrt{3}e^3 K_e}{4mc^2 R^2} \left(\frac{3e}{2\pi m^3 c^5}\right)^{(p-1)/2} \Gamma\left(\frac{3p-1}{12}\right) \Gamma\left(\frac{3p+7}{12}\right) \qquad \text{(A2)}$$

here $I(\nu) = \int \tilde{I}(\mathbf{r}, \nu) R^2 dR d\Omega$ and so on, R is a distance from the point at LOS to the observer. The local averaging of Eq. (A2) over the stochastic magnetic field is done assuming the Gaussian probability distribution function (PDF)

$$dP = P(B_x, B_y) dB_x dB_y = \frac{1}{2\pi\sigma_x\sigma_y} \exp\left(-\frac{B_x^2}{2\sigma_x^2} - \frac{B_y^2}{2\sigma_y^2}\right) dB_x dB_y$$

$$= \frac{1}{2\pi\sigma_x\sigma_y} \exp\left(-\frac{B^2\cos^2(\phi)}{2\sigma_x^2} - \frac{B^2\sin^2(\phi)}{2\sigma_y^2}\right) B dB d\phi \qquad \text{(A3)}$$

The angle ϕ is measured counterclockwise from the Ox axis and $\sigma_x^2 = \langle B_x^2 \rangle$, $\sigma_y^2 = \langle B_y^2 \rangle$. We measure angle χ counterclockwise from the $-Ox$ axis (Fig. 2) so $\chi = \phi + \pi/2$, $\cos\chi = -B_y/B_\perp$, $\sin\chi = B_x/B_\perp$ and the local emission at point P: $\tilde{Q}(\mathbf{r}, t, \nu) \propto (B_y^2 - B_x^2)/B_\perp$, $\tilde{U}(\mathbf{r}, t, \nu) \propto 2B_y \cdot B_x/B_\perp$. After averaging over the magnetic field directions one obtains $\langle \tilde{U}(\mathbf{r}, t, \nu) \rangle = 0$. This means that $U = 0$, and the value of the polarization degree is $\Pi = |Q|/I$. This is a consequence of the problem symmetry and the choice of coordinate axes. The parameters $\sigma_x^2 = \langle B_x^2 \rangle$, $\sigma_y^2 = \langle B_{tr}^2 \rangle/2$,

$q = 2\sigma_y^2/\sigma_x^2$ are functions of the position at LOS. $\sigma_y^2 = \langle \boldsymbol{B}_{tr}^2 \rangle/2$, $\langle B_r^2 \rangle$, $\langle \boldsymbol{B}_{tr}^2 \rangle$ depend on r. $\sigma_x^2 = \langle B_r^2 \rangle \cos^2(\alpha) + \langle \boldsymbol{B}_{tr}^2 \rangle \sin^2(\alpha)/2$, $q = 2\langle B_y^2 \rangle/\langle B_x^2 \rangle = 2q_0/(2\cos^2(\alpha) + q_0\sin^2(\alpha))$ also depend on α—an inclination angle shown on Fig. 1, $tg\alpha = l/\rho$, $q_0 = \langle \boldsymbol{B}_{tr}^2 \rangle/\langle B_r^2 \rangle$.

$$
\langle \tilde{I}(\mathbf{r},\nu) \rangle = W_0 \frac{p+7/3}{p+1} \int_0^\infty \int_{-\pi}^\pi \frac{dB_\perp d\phi}{2\pi\sigma_x\sigma_y} B_\perp^{(p+3)/2} \nu^{-(p-1)/2} \exp\left(-\frac{B_\perp^2 \cos^2(\phi)}{2\sigma_x^2} - \frac{B_\perp^2 \sin^2(\phi)}{2\sigma_y^2} \right)
$$

$$
= \frac{W_0}{4\pi\sigma_x\sigma_y} \frac{p+7/3}{p+1} \Gamma\left(\frac{p+5}{4}\right) \left(\frac{\sigma_y^2+\sigma_x^2}{4\sigma_x^2\sigma_y^2}\right)^{-(p+5)/4} \nu^{-(p-1)/2} \int_{-\pi}^\pi d\phi \left(1 - \frac{\sigma_y^2-\sigma_x^2}{\sigma_y^2+\sigma_x^2}\cos(\phi)\right)^{-(p+5)/4}
$$

$$
\langle \tilde{Q}(\mathbf{r},\nu) \rangle = W_0 \int_0^\infty \int_{-\pi}^\pi \frac{dB_\perp d\phi}{2\pi\sigma_x\sigma_y} B_\perp^{\frac{p+3}{2}} \nu^{-(p-1)/2} \cos(2\phi+\pi) \exp\left(-\frac{B_\perp^2 \cos^2(\phi)}{2\sigma_x^2} - \frac{B_\perp^2 \sin^2(\phi)}{2\sigma_y^2} \right)
$$

$$
= \frac{W_0}{4\pi\sigma_x\sigma_y} \Gamma\left(\frac{p+5}{4}\right) \left(\frac{\sigma_y^2+\sigma_x^2}{4\sigma_x^2\sigma_y^2}\right)^{-(p+5)/4} \nu^{-(p-1)/2} \int_{-\pi}^\pi d\phi \, \cos(\phi) \left(1 - \frac{\sigma_y^2-\sigma_x^2}{\sigma_y^2+\sigma_x^2}\cos(\phi)\right)^{-(p+5)/4}
$$

Taking into account that $q = q(\alpha, r) = 2\sigma_y^2/\sigma_x^2$ one obtains

$$
\langle \tilde{I}(\mathbf{r},\nu) \rangle = \frac{W_0}{\pi 2\sqrt{2}} \frac{p+7/3}{p+1} \Gamma\left(\frac{p+5}{4}\right) \sigma_y^{(p+1)/2} \sqrt{q} \left(\frac{q+2}{8}\right)^{-(p+5)/4} \nu^{-(p-1)/2} \int_0^\pi d\phi \left(1 - \frac{q-2}{q+2}\cos(\phi)\right)^{-\frac{p+5}{4}}
$$

$$
\langle \tilde{Q}(\mathbf{r},\nu) \rangle = \tilde{\Pi}(p,q)\langle \tilde{I}(\mathbf{r},\nu) \rangle
$$

$$
\tilde{\Pi}(p,q) = \frac{p+1}{p+7/3} \frac{\int_0^\pi d\phi \left(1 - \frac{q-2}{q+2}\cos(\phi)\right)^{-(p+5)/4} \cos(\phi)}{\int_0^\pi d\phi \left(1 - \frac{q-2}{q+2}\cos(\phi)\right)^{-(p+5)/4}} \tag{A4}
$$

The polarization degree $|\tilde{\Pi}(p,q)|$ (A4) of the local contribution is a function of only 2 parameters: q and p.

<h2 style="text-align:center">APPENDIX B: FITTING PROCEDURES</h2>

The magnetic field obtained in Sec. IV remains irregular even after averaging over slices of the simulation box with particular x-coordinates. The result of such averaging in the downstream region is shown with red and green curves in Fig. 5, together with a smooth analytic approximations (blue curves). The following functions were used for the approximation:

$$
B_{r,\mu G} = \frac{A_0 \cdot \left[1 + \left(\frac{x-A_3}{A_1}\right)^2\right]^{A_2}}{1 + A_6 \cdot \exp\left(-\frac{x-A_4}{A_5}\right)}
$$

$$
B_{tr,\mu G}/\sqrt{2} = C_0 \cdot \left[1 + \left(\frac{x-C_3}{C_1}\right)^2\right]^{C_2} + C_6 \cdot \exp\left[-\left(\frac{x-C_4}{C_5}\right)^2\right].
$$

The fitting was done in the downstream region with variable coefficients A_i and C_i. The coefficient values obtained for χ^2 minimization are $A_0 = 230.0$, $A_1 = 0.25$, $A_2 = -0.16$, $A_3 = 0.85$, $A_4 = 0.0$, $A_5 = 0.13$, $A_6 = 2.2 \times 10^5$, $C_0 = 137.6$, $C_1 = 0.75$, $C_2 = -0.26$, $C_3 = 1.95$, $C_4 = 1.80$, $C_5 = 0.17$, and $C_6 = 51.5$. All spatial dimension variables are measured in units of L_* with $x = 0$ being the simulation box boundary. The shock position at the end of the simulation is located at $x = 1.8L_*$.

[1] E. A. Helder, J. Vink, A. M. Bykov, Y. Ohira, J. C. Raymond, and R. Terrier, Space Sci. Rev. **173,** 369 (2012).
[2] P. Blasi, Astron. Astrophys. Rev. **21,** 70 (2013).
[3] E. Amato, Int. J. Mod. Phys. D **23,** 1430013 (2014).
[4] R. Blandford, P. Simeon, and Y. Yuan, Nucl. Phys. B, Proc. Suppl. **256,** 9 (2014).
[5] A. M. Bykov, D. C. Ellison, A. Marcowith, and S. M. Osipov, Space Sci. Rev. **214,** 41 (2018).
[6] V. L. Ginzburg and S. I. Syrovatskii, Annu. Rev. Astron. Astrophys. **3,** 297 (1965).
[7] E. Parizot, A. Marcowith, J. Ballet, and Y. A. Gallant, Astron. Astrophys. **453,** 387 (2006).
[8] A. M. Bykov, Y. A. Uvarov, J. B. G. M. Bloemen, J. W. den Herder, and J. S. Kaastra, Mon. Not. R. Astron. Soc. **399,** 1119 (2009).
[9] M. G. Baring, IAU Symp. **331,** 242 (2017).
[10] A. M. Bykov, Y. A. Uvarov, P. Slane, and D. C. Ellison, Astrophys. J. **899,** 142 (2020).
[11] R. Bandiera and O. Petruk, Mon. Not. R. Astron. Soc. **459,** 178 (2016).
[12] O. Petruk, R. Bandiera, V. Beshley, S. Orlando, and M. Miceli, Mon. Not. R. Astron. Soc. **470,** 1156 (2017).
[13] J. R. Dickel, W. J. M. van Breugel, and R. G. Strom, Astron. J. **101,** 2151 (1991).
[14] E. M. Reynoso, D. A. Moffett, W. M. Goss, G. M. Dubner, J. R. Dickel, S. P. Reynolds, and E. B. Giacani, Astrophys. J. **491,** 816 (1997).
[15] D. K. Milne, Aust. J. Phys. **40,** 771 (1987).
[16] S. P. Reynolds and D. M. Gilmore, Astron. J. **106,** 272 (1993).
[17] C. A. Wood, S. L. Mufson, and J. R. Dickel, Astron. J. **103,** 1338 (1992).
[18] P. Soffitta, L. Baldini, R. Bellazzini, E. Costa, L. Latronico, F. Muleri, E. Del Monte, S. Fabiani, M. Minuti, M. Pinchera *et al.*, Astron. J. **162,** 208 (2021).
[19] M. C. Weisskopf, P. Soffitta, L. Baldini, B. D. Ramsey, S. L. O'Dell, R. W. Romani, G. Matt, W. D. Deininger, W. H. Baumgartner, R. Bellazzini *et al.*, J. Astron. Telesc. Instrum. Syst. **8,** 026002 (2022).
[20] J. Vink, D. Prokhorov, R. Ferrazzoli, P. Slane, P. Zhou, K. Asakura, L. Baldini, N. Bucciantini, E. Costa, A. Di Marco *et al.*, Astrophys. J. **938,** 40 (2022).
[21] R. Ferrazzoli, P. Slane, D. Prokhorov, P. Zhou, J. Vink, N. Bucciantini, E. Costa, N. Di Lalla, A. Di Marco, P. Soffitta *et al.*, Astrophys. J. **945,** 52 (2023).
[22] P. Zhou, D. Prokhorov, R. Ferrazzoli, Y.-J. Yang, P. Slane, J. Vink, S. Silvestri, N. Bucciantini, E. Reynoso, D. Moffett *et al.*, Astrophys. J. **957,** 55 (2023).
[23] R. Blandford and D. Eichler, Phys. Rep. **154,** 1 (1987).
[24] M. A. Malkov and L. O. Drury, Rep. Prog. Phys. **64,** 429 (2001).
[25] A. R. Bell, Mon. Not. R. Astron. Soc. **353,** 550 (2004).
[26] B.-I. Jun and M. L. Norman, Astrophys. J. **465,** 800 (1996).
[27] J. M. Blondin and D. C. Ellison, Astrophys. J. **560,** 244 (2001).
[28] V. N. Zirakashvili and V. S. Ptuskin, Astrophys. J. **678,** 939 (2008).
[29] E. Amato and P. Blasi, Mon. Not. R. Astron. Soc. **392,** 1591 (2009).

[30] K. M. Schure, A. R. Bell, L. O'C Drury, and A. M. Bykov, Space Sci. Rev. **173,** 491 (2012).
[31] A. M. Bykov, D. C. Ellison, S. M. Osipov, and A. E. Vladimirov, Astrophys. J. **789,** 137 (2014).
[32] P. O. Lagage and C. J. Cesarsky, Astron. Astrophys. **125,** 249 (1983).
[33] A. Achterberg, R. D. Blandford, and S. P. Reynolds, Astron. Astrophys. **281,** 220 (1994).
[34] A. R. Bell and S. G. Lucek, Mon. Not. R. Astron. Soc. **321,** 433 (2001).
[35] D. Caprioli and A. Spitkovsky, Astrophys. J. **794,** 46 (2014).
[36] L. D. Landau and E. M. Lifshitz, *Fluid Mechanics* (Elsevier, Amsterdam, 1987).
[37] A. M. Bykov, Sov. Astron. Lett. **8,** 320 (1982).
[38] J. Giacalone and J. R. Jokipii, Astrophys. J. Lett. **663,** L41 (2007).
[39] F. Fraschetti, Astrophys. J. **770,** 84 (2013).
[40] M. Lemoine, O. Ramos, and L. Gremillet, Astrophys. J. **827,** 44 (2016).
[41] D. Trotta, F. Pecora, A. Settino, D. Perrone, H. Hietala, T. Horbury, W. Matthaeus, D. Burgess, S. Servidio, and F. Valentini, Astrophys. J. **933,** 167 (2022).
[42] T. Inoue, J. Shimoda, Y. Ohira, and R. Yamazaki, Astrophys. J. Lett. **772,** L20 (2013).
[43] Y. Hu, S. Xu, J. M. Stone, and A. Lazarian, Astrophys. J. **941,** 133 (2022).
[44] J. K. J. Hew and C. Federrath, Mon. Not. R. Astron. Soc. **520,** 6268 (2023).
[45] A. Achterberg and R. D. Blandford, Mon. Not. R. Astron. Soc. **218,** 551 (1986).
[46] J. Giacalone and J. R. Jokipii, Astrophys. J. Lett. **663,** L41 (2007).
[47] F. Guo, J. Giacalone, and L. Zhao, Front. Astron. Space Sci. **8,** 27 (2021).
[48] A. P. Kazantsev, Sov. Phys. JETP **26,** 1031 (1968).
[49] A. Brandenburg and K. Subramanian, Phys. Rep. **417,** 1 (2005).
[50] A. Shukurov and D. Sokoloff, Dynamos, in *Les Houches*, edited by P. Cardin and L. Cugliandolo (Elsevier, New York, 2008), Vol. 88, pp. 251–299, https://www.sciencedirect.com/science/article/pii/S092480990880008X.
[51] S. Xu and A. Lazarian, Astrophys. J. **833,** 215 (2016).
[52] A. Brandenburg, T. Kahniashvili, S. Mandal, A. R. Pol, A. G. Tevzadze, and T. Vachaspati, Phys. Rev. Fluids **4,** 024608 (2019).
[53] B. J. Williams, L. Chomiuk, J. W. Hewitt, J. M. Blondin, K. J. Borkowski, P. Ghavamian, R. Petre, and S. P. Reynolds, Astrophys. J. Lett. **823,** L32 (2016).
[54] B. J. Williams, K. J. Borkowski, P. Ghavamian, J. W. Hewitt, S. A. Mao, R. Petre, S. P. Reynolds, and J. M. Blondin, Astrophys. J. **770,** 129 (2013).
[55] A. Ellien, E. Greco, and J. Vink, Astrophys. J. **951,** 103 (2023).
[56] R. Kobashi, S.-H. Lee, T. Tanaka, and K. Maeda, Astrophys. J. **961,** 32 (2024).
[57] H. Uchida, T. Kasuga, K. Maeda, S.-H. Lee, T. Tanaka, and A. Bamba, Astrophys. J. **962,** 159 (2024).
[58] G. Cassam-Chenaï, J. P. Hughes, J. Ballet, and A. Decourchelle, Astrophys. J. **665,** 315 (2007).

[59] A. Mignone, G. Bodo, S. Massaglia, T. Matsakos, O. Tesileanu, C. Zanni, and A. Ferrari, Astrophys. J. Suppl. Ser. **170,** 228 (2007).

[60] A. M. Bykov, A. Brandenburg, M. A. Malkov, and S. M. Osipov, Space Sci. Rev. **178,** 201 (2013).

[61] P. Slane, S. H. Lee, D. C. Ellison, D. J. Patnaude, J. P. Hughes, K. A. Eriksen, D. Castro, and S. Nagataki, Astrophys. J. **783,** 33 (2014).

[62] S. Fabiani, E. Costa, E. Del Monte, F. Muleri, P. Soffitta, A. Rubini, R. Bellazzini, A. Brez, L. de Ruvo, M. Minuti *et al.,* Astrophys. J. Suppl. Ser. **212,** 25 (2014).

[63] http://cxc.cfa.harvard.edu/ciao/ahelp/psf.html.

[64] C. C. Haggerty and D. Caprioli, Astrophys. J. **905,** 1 (2020).

[65] A. M. Bykov, S. M. Osipov, and D. C. Ellison, Mon. Not. R. Astron. Soc. **410,** 39 (2011).

[66] B. Reville and A. R. Bell, Mon. Not. R. Astron. Soc. **430,** 2873 (2013).

[67] J. A. Gaskin, D. A. Swartz, A. Vikhlinin, F. Özel, K. E. Gelmis, J. W. Arenberg, S. R. Bandler, M. W. Bautz, M. M. Civitani, A. Dominguez *et al.,* J. Astron. Telesc. Instrum. Syst. **5,** 021001 (2019).